

# Characterization of photodamage in coherent anti-Stokes Raman scattering microscopy

Yan Fu<sup>1</sup>, Haifeng Wang<sup>1</sup>, Riyi Shi<sup>1,3</sup>, Ji-Xin Cheng<sup>1,2</sup>

<sup>1</sup>Weldon School of Biomedical Engineering, <sup>2</sup>Department of Chemistry, <sup>3</sup>Department of Basic Medical Sciences, Institute for Applied Neurology, and Center for Paralysis Research, Purdue University, West Lafayette, IN 47907  
[jcheng@purdue.edu](mailto:jcheng@purdue.edu)

**Abstract:** We report a mechanistic analysis of photodamage in coherent anti-Stokes Raman scattering (CARS) microscopy. Photodamage to the myelin sheath in spinal tissues is induced by using the point scan mode and is featured by myelin splitting and shockwaves with broadband emission. Our measurement of photodamage rate versus the excitation power reveals that both linear and nonlinear mechanisms are involved. Moreover, we show that vibrational absorption induced by coherent Raman processes significantly contributes to the nonlinear damage at high peak powers. For CARS imaging of cultured cells, the photodamage is characterized by plasma membrane blebbing and is dominated by a second order mechanism. Our study suggests that for dense samples such as the myelin sheath, CARS imaging induced photodamage can be minimized by using laser beams with relatively long near IR wavelengths and a repetition rate of a few MHz. For less dense samples such as cultured cells, laser pulses of higher repetition rates are preferred.

© 2006 Optical Society of America

**OCIS codes:** (350.1820)Damage; (190.7110)Ultrafast nonlinear optics; (180.5810)Scanning microscopy.

---

## References and links

1. W. Denk, J. H. Strickler, and W. W. Webb, "Two-Photon Laser Scanning Fluorescence Microscopy," *Science* **248**, 73-76 (1990).
2. C. Xu, W. Zipfel, J. B. Shear, R. M. Williams, and W. W. Webb, "Multiphoton fluorescence excitation: new spectral windows for biological nonlinear microscopy," *Proc. Natl. Acad. Sci. USA* **93**, 10763-10768 (1996).
3. L. Moreaux, O. Sandre, and J. Mertz, "Membrane imaging by second-harmonic generation microscopy," *J. Opt. Soc. Am. B* **17**, 1685-1694 (2000).
4. P. J. Campagnola and L. M. Loew, "Second-harmonic imaging microscopy for visualizing biomolecular arrays in cells, tissues and organisms," *Nat. Biotech.* **21**, 1356-1360 (2003).
5. J. X. Cheng and X. S. Xie, "Coherent anti-Stokes Raman scattering microscopy: instrumentation, theory, and applications," *J. Phys. Chem. B* **108**, 827-840 (2004).
6. M. D. Duncan, J. Reintjes, and T. J. Manuccia, "Scanning Coherent Anti-Stokes Raman Microscope," *Opt. Lett.* **7**, 350-352 (1982).
7. A. Zumbusch, G. R. Holtom, and X. S. Xie, "Three-dimensional vibrational imaging by coherent anti-Stokes Raman scattering," *Phys. Rev. Lett.* **82**, 4142-4145 (1999).
8. J. X. Cheng, A. Volkmer, L. D. Book, and X. S. Xie, "An epi-detected coherent anti-Stokes Raman scattering (E-CARS) microscope with high spectral resolution and high sensitivity," *J. Phys. Chem. B* **105**, 1277-1280 (2001).
9. A. Volkmer, J. X. Cheng, and X. S. Xie, "Vibrational imaging with high sensitivity via epi-detected coherent anti-Stokes Raman scattering microscopy," *Phys. Rev. Lett.* **87**, 023901 (2001).
10. G. W. H. Wurpel, J. M. Schins, and M. Müller, "Chemical specificity in three-dimensional imaging with multiplex coherent anti-Stokes Raman scattering microscopy," *Opt. Lett.* **27**, 1093-1095 (2002).
11. J. X. Cheng, A. Volkmer, and X. S. Xie, "Theoretical and experimental characterization of coherent anti-Stokes Raman scattering microscopy," *J. Opt. Soc. Am. B* **19**, 1363-1375 (2002).
12. N. Dudovich, D. Oron, and Y. Silberberg, "Single-pulse coherently controlled nonlinear Raman spectroscopy and microscopy," *Nature* **418**, 512-514 (2002).
13. C. L. Evans, E. O. Potma, and X. S. Xie, "Coherent anti-Stokes Raman scattering spectral interferometry: determination of the real and imaginary components of nonlinear susceptibility  $\chi^{(3)}$  for vibrational microscopy," *Opt. Lett.* **29**, 2923-2925 (2004).

14. K. P. Knutsen, J. C. Johnson, A. E. Miller, P. B. Petersen, and R. J. Saykally, "High spectral resolution multiplex CARS spectroscopy using chirped pulses," *Chem. Phys. Lett.* **387**, 436-441 (2004).
15. T. Ichimura, N. Hayazawa, M. Hashimoto, Y. Inouye, and S. Kawata, "Tip-enhanced coherent anti-Stokes Raman scattering for vibrational nanoimaging," *Phys. Rev. Lett.* **92**, 220801 (2004).
16. J. S. Bredfeldt, C. Vinegoni, D. L. Marks, and S. A. Boppart, "Molecular sensitivity optical coherence tomography," *Opt. Lett.* **30**, 495-497 (2005).
17. P. D. Maker and R. W. Terhune, "Study of Optical effects Due to an Induced Polarization Third Order in the Electric Field Strength," *Phys. Rev.* **137**, A801-818 (1965).
18. Y. R. Shen, *The Principles of Nonlinear Optics* (John Wiley and Sons Inc., New York, 1984).
19. L. Li, H. Wang, and J. X. Cheng, "Quantitative coherent anti-Stokes Raman scattering imaging of lipid distribution in co-existing domains," *Biophys. J.* **89**, 3480-3490 (2005).
20. G. W. H. Wurpel, H. A. Rinia, and M. Müller, "Imaging orientational order and lipid density in multilamellar vesicles with multiplex CARS microscopy," *J. Microsc.* **218**, 37-45 (2005).
21. E. O. Potma and X. S. Xie, "Direct visualization of lipid phase segregation in single lipid bilayers with coherent anti-Stokes Raman scattering microscopy," *Chem. Phys. Chem.* **6**, 77-79 (2005).
22. X. Nan, J. X. Cheng, and X. S. Xie, "Vibrational imaging of lipid droplets in live fibroblast cells using coherent anti-Stokes Raman microscopy," *J. Lipid Res.* **40**, 2202-2208 (2003).
23. C. L. Evans, E. O. Potma, M. Puoris'haag, D. Côté, C. P. Lin, and X. S. Xie, "Chemical imaging of tissue in vivo with video-rate coherent anti-Stokes Raman scattering microscopy," *Proc. Natl. Acad. Sci. USA* **102**, 16807-16812 (2005).
24. J. X. Cheng, S. Pautot, D. A. Weitz, and X. S. Xie, "Ordering of water molecules between phospholipid bilayers visualized by coherent anti-Stokes Raman scattering microscopy," *Proc. Natl. Acad. Sci. USA* **100**, 9826-9830 (2003).
25. E. O. Potma, W. P. D. Boeij, P. J. M. v. Haastert, and D. A. Wiersma, "Real-time visualization of intracellular hydrodynamics in single living cells," *Proc. Natl. Acad. Sci. USA* **98**, 1577-1582 (2001).
26. A. P. Kennedy, J. Sutcliffe, and J. X. Cheng, "Molecular composition and orientation of myelin figures characterized by coherent anti-Stokes Raman scattering microscopy," *Langmuir* **21**, 6478-6486 (2005).
27. H. Wang, Y. Fu, P. Zickmund, R. Shi, and J. X. Cheng, "Coherent anti-Stokes Raman scattering imaging of live spinal tissues," *Biophys. J.* **89**, 581-591 (2005).
28. A. Vogel, J. Noack, G. Huettmann, and G. Paltauf, "Femtosecond-laser-produced low-density plasmas in transparent biological media: a tool for the creation of chemical, thermal, and thermomechanical effects below the optical breakdown threshold," *Proc. SPIE* **4633A**, 1-15 (2002).
29. K. König, "Laser tweezers and multiphoton microscopes in life sciences," *Histochem. Cell Biol.* **114**, 79-92 (2000).
30. A. Hopt and E. Neher, "Highly nonlinear photodamage in two-photon fluorescence microscopy," *Biophys. J.* **80**, 2029-2036 (2001).
31. K. König, T. W. Becker, P. Fischer, I. Riemann, and K.-J. Halbhuber, "Pulse-length dependence of cellular response to intense near-infrared laser pulses in multiphoton microscopes," *Opt. Lett.* **24**, 113-115 (1999).
32. H. J. Koester, D. Baur, R. Uhl, and S. W. Hell, "Ca<sup>2+</sup> fluorescence imaging with pico- and femtosecond two-photon excitation: signal and photodamage," *Biophys. J.* **77**, 2226-2236 (1999).
33. J. S. Gomez, "Coherent Raman Spectroscopy," in *Modern Techniques in Raman Spectroscopy*, J. J. Laserna, editor. (John Wiley & Sons Inc., New York, 1996).
34. P. Morell and R. H. Quarles, "Myelin formation, structure, and biochemistry," in *Basic Neurochemistry: Molecular, Cellular, and Medical Aspects*, G. J. Siegel, B. W. Agranoff, R. W. Alberts, and P. B. Molinoff, eds. (Lippincott Williams & Wilkins, Philadelphia, 1999).
35. P. N. Prasad, *Introduction to biophotonics*. (Wiley Interscience, Hoboken, NJ, 2003), pp. 168-175.
36. J. Diels and W. Rudolph, "Generation of extreme wavelengths," in *Ultrashort laser pulse phenomena: fundamentals, techniques, and applications on a femtosecond time scale*. (Academic Press, San Diego, 1996), pp. 472-475.
37. H. R. Griem, "Optical radiation," in *Plasma physics in theory and application*, W. B. Kunkel, editor. (McGraw-Hill, Inc., New York, 1966), pp. 278-280.
38. K. C. Neuman, E. H. Chadd, G. F. Liou, K. Bergman, and S. M. Block, "Characterization of photodamage to *Escherichia coli* in optical traps," *Biophys. J.* **77**, 2856-2863 (1999).
39. B. R. Masters, P. T. C. So, C. Buehler, N. Barry, J. D. Sutin, W. W. Mantulin, and E. Gratton, "Mitigating thermal mechanical damage potential during two-photon dermal imaging," *J. Biomed. Opt.* **9**, 1265-1270 (2004).
40. Y. Liu, G. J. Sonek, M. W. Berns, and B. J. Tromberg, "Physiological monitoring of optically trapped cells: assessing the effects of confinement by 1064-nm laser tweezers using microfluorometry," *Biophys. J.* **71**, 2158-2167 (1996).
41. H. Wang, Y. Fu, and J. X. Cheng, "Light-matter energy exchange in coherent Raman microscopy," *Phys. Rev. A*, submitted (2005).
42. K. König, H. Liang, M. W. Berns, and B. J. Tromberg, "Cell damage in near-infrared multimode optical traps as a result of multiphoton absorption," *Opt. Lett.* **21**, 1090-1092 (1996).

43. M. L. Cunningham, J. S. Johnson, S. M. Giovanazzi, and M. J. Peak, "Photosensitized production of superoxide anion by monochromatic (290-405 nm) ultraviolet irradiation of NADH and NADPH coenzymes," *Photochem. Photobiol.* **42**, 125-128 (1985).
- 

## 1. Introduction

Nonlinear optical (NLO) imaging techniques including two photon excitation fluorescence (TPEF) [1, 2], second harmonic generation (SHG) [3, 4], and coherent anti-Stokes Raman scattering (CARS) microscopy [5], have opened a new window for 3D imaging of biological samples. Among these tools, CARS microscopy permits molecular imaging without any labeling [6-16]. CARS is a four-wave mixing process in which the interaction of a pump field  $E_p(\omega_p)$  and a Stokes field  $E_s(\omega_s)$  with a sample generates an anti-Stokes field  $E_{as}$  at frequency  $2\omega_p - \omega_s$  [17, 18]. The CARS signal is significantly enhanced when  $\omega_p - \omega_s$  is tuned to a Raman band, creating the vibrational contrast. The coherent addition of CARS fields from the vibrational oscillators in the focal volume results in a large signal, permitting molecular imaging with a high speed. CARS microscopy has been used to study a broad range of biological samples including lipid bilayers [19-21], lipid droplets [22], skin [23], biological water [24, 25], myelin figures [26], and neuronal myelin sheath [27].

Ultrashort laser pulses with high peak power are needed for efficient signal generation in NLO microscopy. The strong intensity at the focal center may generate plasma through multiphoton processes and destruct the biological sample [28, 29]. TPEF studies of cells with femtosecond (fs) laser pulses [30, 31] suggested that two-photon electronic absorption was the main photodamage mechanism at low excitation powers and higher order processes might occur at larger excitation powers [32]. So far no photodamage study has been reported for CARS microscopy. The photodamage mechanisms in CARS microscopy could be different from those in TPEF microscopy for the following reasons. First, fs pulses are widely used in TPEF imaging, while CARS imaging usually uses picosecond (ps) pulses because their spectral width matches most Raman bands [8]. Second, vibrational absorption occurs in CARS microscopy through coherent Raman processes [33], which may contribute to additional damage.

The goal of this paper is to characterize the photodamage in CARS microscopy and further identify the optimal laser parameters to minimize it. One biological sample used in our study was isolated spinal cord white matter segment containing largely myelinated axons. Axonal myelin contains a large content of lipids (70% of dry weight) [34]. The high-density  $\text{CH}_2$  groups in myelin produce a large resonant CARS signal at symmetrical  $\text{CH}_2$  stretching frequency of  $2840 \text{ cm}^{-1}$ . Recently we have applied CARS microscopy to image axonal myelin of live spinal tissues in its natural state [27]. Under the normal scan speed of 1.1 second/frame and laser repetition rate of 3.9 to 7.8 MHz, very little photodamage was observed during CARS imaging. To intentionally induce damage to the myelin sheath, we used the point scan mode of the microscope in which the foci of two excitation beams were fixed on the sample during scanning. The photodamage rate, defined as the inverse of the time needed to induce damage, was measured to analyze the effects of various parameters including laser power, Raman shift, excitation wavelengths, and repetition rate. The phenomena and mechanisms of photodamage in CARS imaging of live cells have also been studied.

## 2. Materials and methods

### 2.1 Sample preparation

Fresh spinal cord samples were prepared following the procedure in [27]. The isolated ventral white matter strip from guinea pig was mounted on a chambered glass coverslip and kept in oxygen bubbled Krebs' solution (NaCl 124 mM, KCl 2 mM,  $\text{KH}_2\text{PO}_4$  1.2 mM,  $\text{MgSO}_4$  1.3 mM,  $\text{CaCl}_2$  2 mM, dextrose 10 mM,  $\text{NaHCO}_3$  26 mM, and sodium ascorbate 10 mM).

## 2.2 CARS microscopy

A schematic of our microscope can be found in [27]. The pump and Stokes laser beams were generated by two tightly synchronized (Sync-Lock) ps Ti:sapphire oscillators (Mira 900, Coherent Inc., Santa Clara, CA). The pump and Stokes laser wavelengths were about 704 nm and 880 nm, respectively, with a pulse width of 2.5 ps. A Pockels' cell was placed in the laser beams to reduce the repetition rate. The laser beams were collinearly combined and directed into a laser scanning confocal microscope (FV300/IX70, Olympus America Inc., Melville, New York). A 60X water immersion objective (numerical aperture (NA)=1.2) was used to focus the excitation beams into the sample. The forward-detected CARS (F-CARS) signal was collected by an air condenser (NA=0.55), while the epi-detected CARS (E-CARS) signal was collected by the same water immersion objective. Both E-CARS and F-CARS signals were detected with photomultiplier tubes. All experiments were conducted at room temperature of 22°C.

## 3. Results and discussion

### 3.1 Photodamage in CARS imaging of myelin sheath

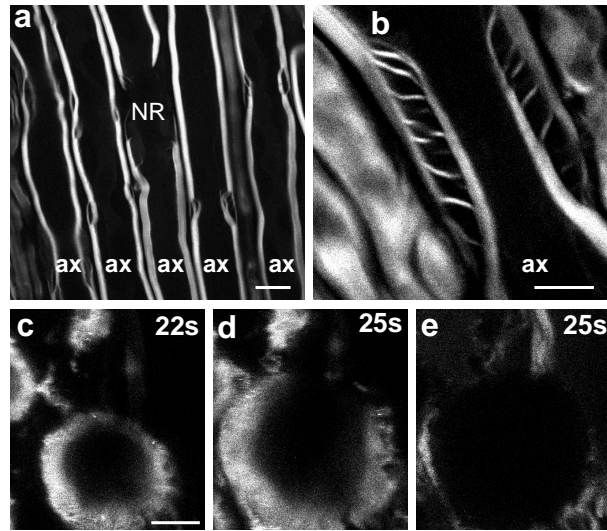


Fig. 1. CARS images of myelin sheath in spinal tissue. (a) Normal myelin sheath wrapping five parallel axons labeled as "ax". The middle axon displays a node of Ranvier (NR). Bar = 10  $\mu\text{m}$ . (b) A Schmidt-Lanterman incisure. Bar = 5  $\mu\text{m}$ . The images in (a-b) were acquired with the peak pump and Stokes power of 323 W and 129 W, respectively. (c) E-CARS image of a damaged site acquired after x-y scanning for 22 s. (d) E-CARS and (e) F-CARS images of the same damaged site as in (c) acquired after x-y scanning for 25 s. The damage shown in (c-e) was induced with peak pump and Stokes power of 74 W and 60 W, respectively.  $f = 39$  MHz. Bar = 5  $\mu\text{m}$  for images (c-e).

With  $\omega_p - \omega_s$  tuned to the peak of the  $\text{CH}_2$  vibration band at  $2840 \text{ cm}^{-1}$ , the myelin sheath displays high contrast in both F-CARS and E-CARS images [27]. Fig. 1(a) shows five parallel axons wrapped by compact myelin sheath. A node of Ranvier was observed in the middle axon. With a lateral resolution of  $0.28 \mu\text{m}$  and an axial resolution of  $0.70 \mu\text{m}$  [27], the lateral loops in Schmidt-Lanterman incisure were clearly resolved (Fig. 1(b)). These high quality images were acquired with an average of 3 scans at a speed of 1.1 second/frame. The laser repetition rate was 7.8 MHz and the average power in the sample was about 8.8 mW. No photodamage was observed under these conditions.

When the laser excitation power was increased to a certain degree and the scan time was long enough, photodamage could be observed. Fig. 1(c) and (d) show the E-CARS images of a damaged site after continuous scanning for 22 s and 25 s, respectively. The average power was 13 mW. The damage was characterized by bright ring-shape emission expanding with time. In the epi-channel, this emission could be detected with filters of different transmissions and with only one excitation beam, indicating that it is a broadband luminescence. The damaged site appeared as a dark hole in the F-CARS image (Fig. 1(e)) because of the low NA of the air condenser used for forward detection.

This kind of photodamage featured by shockwaves and cavitation is referred as photodisruption [35]. Under high laser power density ( $\sim 2 \times 10^{11}$  W/cm<sup>2</sup> in our case), one- and multi-photon processes could ionize the tissue and generate a plasma [36] which could break chemical bonds and induce localized ablation [28]. The high-density plasma strongly absorbs laser energy and generates shockwaves which disrupt the tissue by a mechanical impact [35]. The collision of free electrons with atoms and ions or recombination of electrons and ions in plasma leads to continuum emission [37].

### 3.2 Point scan induced photodamage

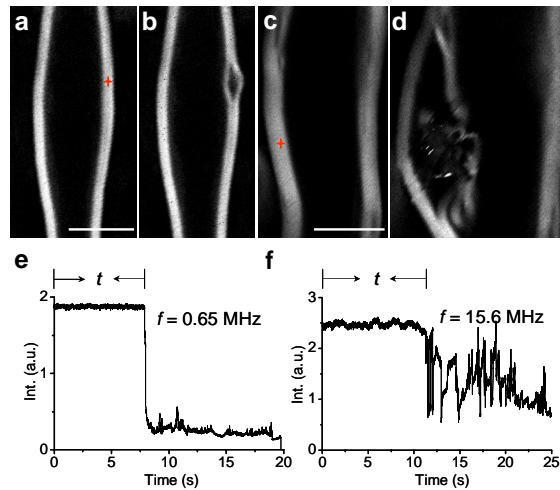


Fig. 2. CARS images of single myelin sheath before and after photodamage induced by point scanning. The x-y imaging and point scanning were carried out at the same condition. (a-b) results with high peak power of the pump (308 W) and Stokes (149 W) beams.  $f = 0.65$  MHz. (e) Intensity trace of point scanning at the position indicated by the red star in (a). (c-d) results with low peak power of the pump (38 W) and Stokes (19 W) beams.  $f = 15.6$  MHz. (f) Intensity trace of point scanning at the position indicated by the red cross in (c). For all images, bar = 5  $\mu$ m.

In the point scan mode the laser foci were fixed on the myelin sheath, and the E-CARS intensity from the foci was recorded as a trace over time. The photodamage induced by point scanning tore the myelin sheath apart (Fig. 2(b, d)) and the signal at the focal point dropped abruptly (Fig. 2(e, f)). The phenomena of damage were found to be dependent on the pulse peak power and the repetition rate  $f$ . At  $f = 0.65$  MHz and high peak powers (pump: 308 W; Stokes: 154 W), the damage was featured by myelin splitting (Fig. 2(b)). The damage was probably initiated by plasma induced ablation [28, 35], following which the plasma further absorbed laser power, expanded, and split the myelin. At  $f = 15.6$  MHz and relatively low peak powers (pump: 38 W; Stokes: 19 W), bursts of signal after initial damage were observed in addition to myelin splitting, as shown in the E-CARS image (Fig. 2(d)) and the intensity trace (Fig. 2(f)). Because the average laser power used at  $f = 15.6$  MHz was 3 times higher

than the power used at  $f = 0.65$  MHz, the plasma could absorb more laser power and produce bursts of emission.

Using the point scan mode we were able to induce photodamage to the myelin sheath repeatedly with specific laser powers and repetition rate. In the following, we use this method to study the mechanisms underlying the observed photodamage and determine the optimal experimental parameters for CARS imaging. We measure the photodamage rate under different conditions to dissect the roles of various laser parameters in the induction of photodamage. The photodamage rate ( $R$ ) is defined as the inverse of the time ( $t$ ) from scan start to the initial intensity dropping (Fig. 2(e, f)). The average photodamage rate of at least ten measurements was obtained under each experimental condition.

### 3.3 Dependence of photodamage rate on excitation power

We first measured the photodamage rate at different excitation powers to determine the order of the damages. It has been claimed that the photodamage rate  $R$  is related to the laser peak power  $P_p$  by  $R \propto P_p^n f \tau$ , where  $f$  is the repetition rate;  $\tau$  is the laser pulse width;  $n$  is the order of underlying mechanism [30]. The measured dependence of photodamage rate on the total excitation power is shown in Fig. 3. In this experiment, the ratio of pump to Stokes power was kept at 3.2.  $f$  was kept at 3.9 MHz. With the total peak power in the range of 97 to 219 W, the measured photodamage rate increased nearly linearly with the total excitation peak power with  $n = 1.10$ . With the total peak power in the range of 219 to 363 W,  $n$  was increased to 1.81. These results indicate the involvement of both linear and second order damages. Additionally, using a 705 nm continuous-wave (CW) laser beam with an average power of 11.5 mW, we could also induce similar damage on the myelin sheath by the point scan mode, further supporting the existence of linear damage.

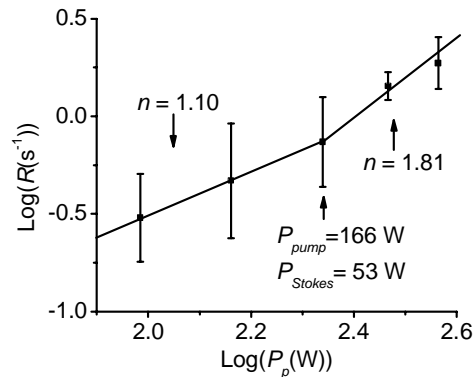


Fig. 3. Dependence of photodamage rate on the total excitation peak power on the sample.  $f = 3.9$  MHz. The power ratio of pump to Stokes lasers was kept constant at 3.2. The peak power of the pump and Stokes beams were adjusted from 74 W to 277 W and from 23 W to 86 W, respectively.

Both linear and nonlinear damages have been reported in the literature. One-photon absorption was suggested to be responsible for the linear damage observed in optical trap study of cells with 870 nm or 1064 nm CW lasers [38]. Photodamage was found to associate with the linear absorption of melanin granules in two-photon skin imaging [39]. Two-photon absorption was suggested as a major second order mechanism for damage in TPEF microscopy using ultrashort near IR laser sources [30-32, 40]. For example,  $n = 2.5$  was obtained in the TPEF imaging study of bovine adrenal chromaffin cells with a 190 fs laser source [30]. In our CARS setup both laser sources had a pulse width of 2.5 ps. The relatively lower pulse peak power could account for the coexistence of both linear and nonlinear

damage in our CARS experiments. In addition, as shown below, we have identified a new second order photodamage mechanism that results from coherent Raman induced vibrational absorption.

### 3.4 Coherent Raman induced photodamage

In CARS microscopy various coherent Raman processes including CARS, coherent Stokes Raman scattering, stimulated Raman gain (SRG), and stimulated Raman loss (SRL) occur simultaneously [18]. Recently Wang *et al.* have shown that coherent Raman processes can induce vibrational absorption in the sample in the presence of Raman resonance [41]. The absorption is principally caused by SRG and SRL due to their heterodyne nature. Accordingly the absorbed power is proportional to the product of the pump and Stokes laser power. Calculations have shown that tight focusing of the incident beams with a high NA objective further enhances this Raman-induced absorption to 0.01% of the input power which is large enough to cause photodamage [41].

The coherent Raman induced damage has been confirmed by our experiment. We fixed the pump laser wavelength and peak power at 701nm/338 W. The Stokes laser has a fixed peak power of 202 W while its wavelength was 843 nm, 857 nm, 875nm and 888 nm for the Raman shift of 2400  $\text{cm}^{-1}$ , 2600  $\text{cm}^{-1}$ , 2840  $\text{cm}^{-1}$  and 3000  $\text{cm}^{-1}$ , respectively. The photodamage rate at Raman resonance (2840  $\text{cm}^{-1}$ ) was two times of that off Raman resonance (Fig. 4(a)). Based on the wavelength dependence study in the next section, longer wavelength laser induces less damage. Therefore, we attribute the enhanced photodamage at 2840  $\text{cm}^{-1}$  to Raman resonance enhanced absorption but not the variation of the Stokes laser wavelengths.

In another experiment with  $f = 15.6$  MHz and low peak powers (pump: 32 W; Stokes: 19 W), the photodamage rate was found to be the same either on or off Raman resonance (Fig. 4(b)). These results indicate that with high peak powers coherent Raman induced absorption significantly contributed to the damage, while with low peak powers it was reduced to a negligible level. Because both second order processes including coherent Raman induced vibrational absorption and two-photon electronic absorption were suppressed simultaneously, linear photodamage prevailed in the low peak power region, as shown in Fig. 3.

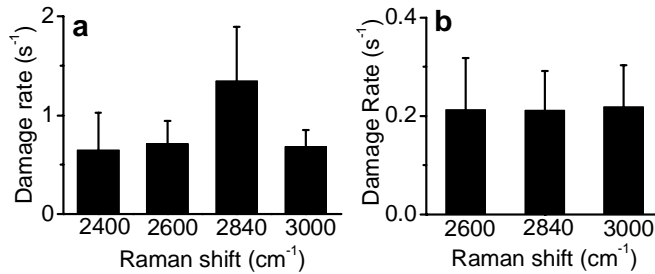


Fig. 4. Dependence of photodamage rate on the Raman shift. The pump wavelength was fixed at 701 nm and the Stokes beam was tuned to generate different Raman shifts. (a) Significant dependence observed with high peak powers of pump (338 W) and Stokes (203 W) beams at  $f = 1.3$  MHz. (b) No dependence observed at low peak powers of pump (32 W) and Stokes (19 W) beams at  $f = 15.6$  MHz.

To minimize the damage in CARS imaging of myelin sheath, below we study the dependence of the photodamage rate on the excitation wavelength and repetition rate.

### 3.5 Dependence of photodamage rate on excitation wavelength

In our CARS imaging experiments, the pump and Stokes wavelengths were around 704 and 880 nm, respectively. To determine which laser beam was more prominent in the photodamage processes, we varied the pump to Stokes power ratio from 0.37 to 2.0 and measured the corresponding photodamage rate. The experiments were performed at  $f = 3.9$  MHz. The total average power was adjusted to maintain a constant CARS signal from myelin sheath. The photodamage rate with pump to Stokes power ratio of 2 was found to be 3.68 times of that with the power ratio of 0.37 (Fig. 5(a)). Because the CARS signal has a quadratic dependence on the pump power and a linear dependence on the Stokes power, for a larger pump to Stokes power ratio the total power was decreased to keep the CARS signal invariant. Thus, a larger pump to Stokes power ratio accelerated the photodamage although the total power was lowered. Similar result was observed in optical traps, wherein shorter wavelength NIR beams induced cell damage more efficiently [42].

We have also studied the wavelength dependence of linear photodamage rate with a single excitation laser on myelin sheath. Based on Fig. 3, we fixed the laser peak power at 50 W on the sample, so that linear mechanism dominates photodamage. The laser repetition rate was 39 MHz. Point scan was still used to induce photodamage. As no CARS signal was generated with a single excitation beam, the bright plasma emission was used to identify the onset of photodamage. We found that the myelin could be damaged within one minute with  $<760$  nm excitation, however with wavelengths from 780-880 nm we could no longer see photodamage within 5 min. Because the water absorption is known to be peaked at 740, 840 and 970 nm, our results suggest that water absorption plays little role in linear photodamage of myelin sheath.

Our observations indicate that excitation with longer wavelengths helps to photodamage in CARS microscopy. On the other hand, the use of longer wavelengths lowers the image resolution and may increase linear absorption of water. This tradeoff must be considered to acquire good image quality and minimize the photodamage at the same time.

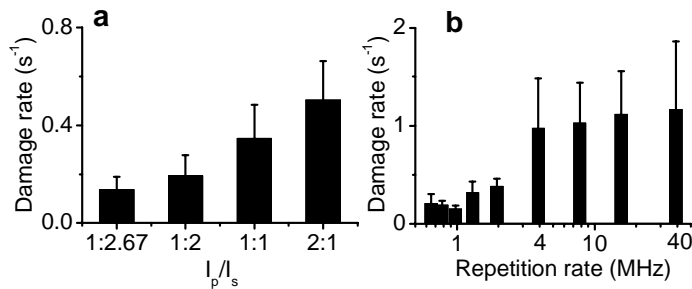


Fig. 5. (a) Dependence of photodamage rate on the pump to Stokes power ratio under the condition of constant CARS signal.  $f = 3.9$  MHz. (b) Dependence of photodamage rate on the repetition rate under the condition of constant CARS signal. The power ratio of pump to Stokes was fixed at 2.  $f$  was varied from 0.65 to 39 MHz. To maintain the same CARS signal at different repetition rates, the pump peak power was changed from 286 W to 52 W and the Stokes peak power from 143 W to 26 W accordingly.

### 3.6 Dependence of photodamage rate on repetition rate

Under the condition of constant CARS signal and fixed pump to Stokes power ratio at 2, we measured the photodamage rates at different pulse repetition rates. The photodamage rate was found to be the lowest at  $f = 0.975$  MHz (Fig. 5(b)). It increased significantly when increasing the repetition rate and increased slightly when lowering the repetition rate. The increase of

photodamage rate in the  $f > 0.975$  MHz region can be explained by the equation  $R \propto P_p^n f \tau$  [30]. The condition of constant CARS signal in our experiments means a constant value of  $P_p^3 f$ , where  $P_p$  is the total laser peak power. The photodamage rate ( $R \propto P_p^n f \tau$ ) caused by linear processes is proportional to  $P_p f \propto f^{2/3}$ , and that caused by second order processes is proportional to  $P_p^2 f \propto f^{1/3}$ , both of which increase with higher repetition rates. The slight increase of photodamage rate in the  $f < 0.975$  MHz region in Fig. 5(b) can be explained by leaked laser power through the Pockels' cell which was used to reduce laser repetition rate by suppressing unwanted pulses. However about 1% of the suppressed pulses were leaked through it. These leaked pulses contributed very little to the CARS signal but added a significant amount of average laser power at the sample when a low repetition rate was used. Without any leakage the average laser power (proportional to  $P_p f \propto f^{2/3}$ ) should decrease at lower repetition rate, but experimentally the total average power at 0.65 MHz was measured to be 0.70 mW, larger than the measured power of 0.69 mW at 0.975 MHz. We believe that the increased laser leakage accounts for the increased photodamage rate through the linear mechanism in the  $f < 0.975$  MHz region.

In general the optimal repetition rate depends on the order of photodamage mechanism. In TPEF microscopy, when damage is caused by linear absorption [39], low repetition rate is preferable because high peak power and low average power excitation can provide good TPEF efficiency and suppress linear absorption at the same time. If damage is caused by two-photon absorption which has the same order as the imaging method [31], under the condition of constant TPEF signal the damage should be insensitive to repetition rate. If the photodamage mechanism is of higher order than the imaging method [30], high repetition rate should be preferable. In our CARS experiments, lowering the repetition rate reduced the photodamage rate because the observed damage has lower order than the CARS process (third order). We would mention that very high pulse peak power at very low repetition rate (e.g. a few KHz) may induce even higher order damage to the sample. Additionally very low repetition rate does not allow high speed scanning. For our CARS system, repetition rates between 1 MHz and 4 MHz are optimal.

### 3.7 Photodamage in CARS imaging of live cells

For photodamage of myelin sheath, plasma generation usually occurs due to the high packing density of molecules in the sample. We have also studied less dense samples such as cultured cells. To characterize the photodamage in CARS imaging of cells, we continuously scan a  $29.4 \times 29.4 \mu\text{m}^2$  area containing live KB cells (Fig. 6(a)). The pump to Stokes peak power ratio is kept at 3.8 and the repetition rate is kept at 7.8 MHz. With the maximum laser peak intensity of  $0.76 \text{ TW/cm}^2$  for the pump and  $0.21 \text{ TW/cm}^2$  for the Stokes, the photodamage usually does not generate plasma. Instead, the damaged cell often shows blebbing of the plasma membrane as in Fig. 6(b). With the full pump and Stokes peak power of 373 W and 101 W at the cell respectively (the total average power is 9.24 mW), it took about one minute to induce blebbing. When the pump and Stokes peak power are 92.3 W and 24 W (the total average power is 2.3 mW), the damage is not observed even after 10 min continuous scanning of the same size of area. Therefore, laser scanning CARS microscopy is generally safe for imaging live cells as an image can be acquired in one second. The time needed to induce blebbing is recorded and its inverse is used as the photodamage rate. The dependence of the photodamage rate on the excitation power is plotted in Fig. 6(c). The data are fitted using the model  $R \propto P_p^n f \tau$  with  $n = 2.29$ , indicating a second-order damage mechanism. The observed nonlinear damage is probably due to two-photon excitation of endogenous cellular absorbers which generate oxygen radicals and singlet oxygen and further induce cell apoptosis [43]. In a control experiment using the CW mode of our Ti:sapphire lasers at the same wavelengths, we

did not see any blebbing in 10 min at the total average power of 9.24 mW. Therefore, being different from the highly dense myelin sample, linear absorption of near IR beam is negligible for the cultured cells.

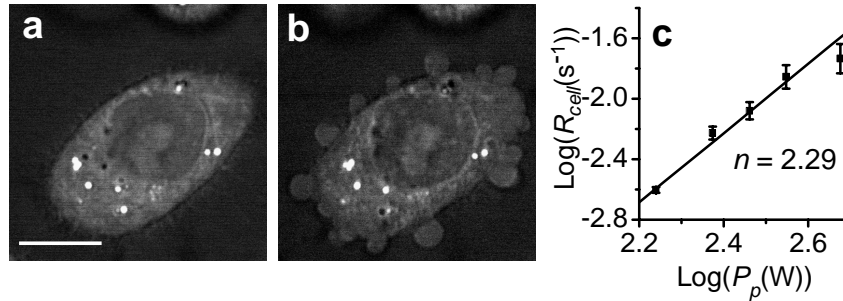


Fig. 6. Photodamage in CARS imaging of live KB cells. (a) CARS image of a KB cell under normal conditions. (b) CARS image of the same KB cell after 3min of scanning with the pump peak power 373W and Stokes peak power 101W. Bar = 10  $\mu\text{m}$ . (c) Dependence of photodamage rate on the total excitation peak power.  $f = 7.8$  MHz. The power ratio of pump to Stokes lasers was kept at 3.8. The peak power of the pump and Stokes beams were adjusted from 138.4 W to 373 W and from 36 W to 101 W, respectively.

#### 4. Conclusions

We have performed a systematic study on the photodamage in CARS imaging of live spinal tissues with two Ti:sapphire lasers with a 2.5 ps pulse width. The photodamage was featured by plasma induced myelin splitting and shockwave generation with broadband emission. We have measured the photodamage rate induced by point scanning under different excitation conditions. With a pump to Stokes power ratio of 3.2 to 1.0, our results show that both linear and second order mechanisms are involved within the total peak power range from 97 W to 363 W, and that the linear mechanism prevails at total peak power lower than 219 W. At high laser peak powers, we found an important second order photodamage mechanism that is due to coherent Raman induced vibrational absorption. Under the condition of constant CARS signal, excitation with longer near IR wavelength and repetition rate of a few MHz reduces the photodamage. For CARS imaging of cultured cells, the photodamage is characterized by plasma membrane blebbing and is dominated by a second order mechanism. Our results provide a guideline to acquire high quality CARS images while minimizing photodamage on biological samples.

#### Acknowledgments

This work was supported by NSF grant #0416785-MCB, NIH R21 grant # EB004966-01 and funding from the State of Indiana. We acknowledge Kristin Hamann and Gary Leung for their kind help in tissue preparation and Hongtao Chen for culturing the KB cells.